A molecularly engineered, broad-spectrum anti-coronavirus lectin inhibits SARS-CoV-2 and MERS-CoV infection *in vivo*

David Markovitz (dmarkov@med.umich.edu)
University of Michigan
Jasper Chan
The University of Hong Kong https://orcid.org/0000-0001-6336-6657
Yoo Jin Oh
Johannes Kepler University of Linz https://orcid.org/0000-0002-9636-3329
Shuofeng Yuan
The University of Hong Kong
Hin Chu
University of Hong Kong
Man Lung Yeung
The University of Hong Kong
Daniel Canena
Johannes Kepler University Linz
Chris Chan
The University of Hong Kong
Vincent Poon
The University of Hong Kong
Chris Chan
The University of Hong Kong
Jinxia Zhang
The University of Hong Kong https://orcid.org/0000-0002-5087-3614
Jian-Piao Cai
The University of Hong Kong
Lei Wen
The University of Hong Kong
Kenn Ka Heng Chik
State Key Laboratory of Emerging Infectious Diseases, Carol Yu Centre for Infection, Department of Microbiology, Li Ka Shing Faculty of Medicine, The University of Hong Kong
Huiping Shuai
The University of Hong Kong

Yixin Wang
The University of Hong Kong
Yuxin Hou
The University of Hong Kong
Cuiting Luo
The University of Hong Kong
Wan-Mui Chan
The University of Hong Kong
Ko-Yung Sit
The University of Hong Kong https://orcid.org/0000-0001-6289-663X
Wing-Kuk Au
University of Hong Kong https://orcid.org/0000-0002-6196-7317
Maureen Legendre
University of Michigan
Rong Zhu
Johannes Kepler University Linz
Lisa Hain
Johannes Kepler University Linz
Kelvin To
The University of Hong Kong https://orcid.org/0000-0002-1921-5824
Kwok-Hung Chan
The University of Hong Kong https://orcid.org/0000-0003-1771-8249
Dafydd Thomas
University of Michigan
Miriam Klausberger
University of Natural Resources and Life Sciences
Johannes Stadlmann
IMBA
Josef Penninger
University of British Columbia https://orcid.org/0000-0002-8194-3777
Chris Oostenbrink
University of Natural Resources and Life Sciences
Peter Hinterdorfer
Johannes Kepler University of Linz https://orcid.org/0000-0003-2583-1305
Kwok-Yung Yuen
The University of Hong Kong https://orcid.org/0000-0002-2083-1552

Biological Sciences - Article

Keywords: Antivirals, High-Mannose, Time-of-drug-addition Assay, Virus Entry, Real-time Structural Analysis, SARS-CoV-2 Spike Trimer

Posted Date: May 17th, 2021

DOI: https://doi.org/10.21203/rs.3.rs-516695/v1

Abstract

Coronaviruses have repeatedly crossed species barriers to cause epidemics[1]. “Pan-coronavirus” antivirals targeting conserved viral components involved in coronavirus replication, such as the extensively glycosylated spike protein, can be designed. Here we show that the rationally engineered H84T-banana lectin (H84T-BanLec), which specifically recognizes high-mannose found on viral proteins but seldom on healthy human cells[2], potently inhibits the highly virulent MERS-CoV, pandemic SARS-CoV-2 and its variants, and other human-pathogenic coronaviruses at nanomolar concentrations. MERS-CoV-infected human DPP4-transgenic mice treated by H84T-BanLec have significantly higher survival, lower viral burden, and reduced pulmonary damage. Similarly, prophylactic or therapeutic H84T-BanLec is effective against SARS-CoV-2 in hamsters. Importantly, intranasally and intraperitoneally administered H84T-BanLec are comparably effective. Time-of-drug-addition assay shows that H84T-BanLec targets virus entry. Real-time structural analysis with high-speed atomic force microscopy depicts multi-molecular associations of H84T-BanLec dimers with the SARS-CoV-2 spike trimer. Single-molecule force spectroscopy demonstrates binding of H84T-BanLec to multiple SARS-CoV-2 spike mannose sites with high affinity, and that H84T-BanLec competes with SARS-CoV-2 spike for binding to cellular ACE2. Modelling experiments identify distinct high-mannose glycans in spike recognized by H84T-BanLec. The multiple H84T-BanLec binding sites on spike likely account for the activity against SARS-CoV-2 variants and the lack of resistant mutants. The broad-spectrum H84T-BanLec should be clinically evaluated in respiratory viral infections including COVID-19.

Introduction

Coronaviruses are enveloped, positive-sense, single-stranded RNA viruses that have repeatedly crossed species barriers from animals to human[1]. Of the four genera in the genetically diverse *Coronaviridae* family (α, β, γ, and d coronaviruses)[1], three novel coronaviruses have emerged to cause epidemics or pandemics in humans: severe acute respiratory syndrome coronavirus (SARS-CoV) in 2002-2003, Middle East respiratory syndrome coronavirus (MERS-CoV) since 2012, and SARS-CoV-2 since 2019[3-6]. SARS and MERS frequently manifest as severe disease with high case-fatality rates of around 10% and 35%, respectively[7,8], and Coronavirus Disease 2019 (COVID-19) caused by SARS-CoV-2 has caused more than 3 million deaths worldwide as of 25 April 2021[9]. Moreover, circulating common cold human coronaviruses (HCoV) including HCoV-OC43, HCoV-229E, HCoV-NL63, and HCoV-HKU1 contribute notably to morbidity, especially in the elderly and immunocompromised[10].

Despite the clinical and public health importance of these coronaviruses, effective anti-coronaviral treatment options remain scarce. Broad-spectrum antivirals such as remdesivir, interferons, ribavirin, lopinavir, and clofazimine have shown variable anti-coronaviral activities against one or more of these CoVs in *in vitro* settings and/or *in vivo*[11-14]. Monoclonal or single-domain antibodies are highly active *in vitro* and/or *in vivo*, but are generally virus- or even strain-specific[15,16]. Convalescent plasma may be useful in severe disease, but was recently shown not to improve the overall mortality of severe COVID-19

patients when started 8 days after symptom onset[17]. Importantly, the development of novel specific antiviral agents and preparation of convalescent plasma are time-consuming and inevitably lags behind highly transmissible pandemics such as COVID-19[10]. Treatment options for the existing coronaviruses and emerging novel coronaviruses should be expanded by finding broad-spectrum antiviral agents that have “pan-coronaviral” activities.

Coronaviruses each possess four major structural proteins, namely the spike, envelope, membrane, and nucleocapsid proteins[18]. The membrane-anchored spike glycoprotein is crucial for virus-cell membrane fusion and cell entry[18]. Lectins are carbohydrate-binding proteins widely found in nature and some have potential antiviral activities[2]. Clinical use of lectins, however, was limited in part by potential side effects mediated by lectin-induced mitogenicity[2]. Banana lectin (BanLec) is a jacalin-related lectin isolated from the fruit of bananas (*Musa acuminata*)[19]. We have previously engineered a BanLec that has preserved broad-spectrum antiviral potency with significantly reduced mitogenicity by introducing a single amino acid substitution to replace histidine 84 with a threonine (H84T-BanLec)[2]. H84T-BanLec exhibits potent broad-spectrum *in vitro* and *in vivo* activities against viruses with high-mannose N-glycans, including human immunodeficiency viruses 1 and 2, influenza viruses A and B, Ebola virus, and hepatitis C virus, by binding to highly glycosylated viral proteins to block attachment, entry, membrane fusion, and/or additional steps in the viral replication cycle[2,19-21]. In this study, we report the pan-coronaviral antiviral activity of H84T-BanLec against human-pathogenic coronaviruses, including its *in vivo* protection against SARS-CoV-2 and MERS-CoV, through binding with the glycosylated viral spike protein to inhibit virus entry into cells. Further, we used atomic force microscopy and molecular modelling to capture the molecular interactions of H84T-BanLec with SARS-CoV-2 spike protein.

Results

Pan-coronaviral antiviral activity of H84T-BanLec

To investigate whether H84T-BanLec possesses pan-coronaviral antiviral activity, we included the highly virulent MERS-CoV (lineage C betacoronavirus), the pandemic SARS-CoV-2 (lineage B betacoronavirus), SARS-CoV (lineage B betacoronavirus), HCoV-OC43 (lineage A betacoronavirus), and HCoV-229E (alphacoronavirus) to represent all the subgroups of human-pathogenic coronaviruses. H84T-BanLec significantly reduced MERS-CoV (**Fig. 1a**) and SARS-CoV-2 (**Fig. 1b**) RNA load in a dose-dependent manner *in vitro*. The mean viral load of MERS-CoV was reduced by 3.30 (Huh-7) to 7.11 (Calu-3) $\log_{10}$copies/ml and that of SARS-CoV-2 was reduced by 3.46 (Caco-2) $\log_{10}$copies/ml, respectively, at 90nM of H84T-BanLec. At ≥10nM, H84T-BanLec completely inhibited infectious plaque formation of MERS-CoV (**Fig. 1c**) and SARS-CoV-2 (**Fig. 1d**). The half maximal effective concentrations (EC_{50}) of H84T-BanLec against MERS-CoV and SARS-CoV-2 were 4.44nM and 6.02nM with selectivity indices [50% cytotoxic concentration (CC_{50})/EC_{50}] of ≥2252.3 and ≥1661.1, respectively (**Extended Data Fig. 1**). In the cytopathic effect (CPE) inhibition assay, dose-dependent reduction of CPE could be consistently observed for both MERS-CoV (>80% in Vero and 100% in Calu-3 cells with ≥30.00nM of H84T-BanLec) (**Fig. 1e**) and

SARS-CoV-2 (>80% in VeroE6 cells) (**Fig. 1f**) at 3 days post-infection (dpi). Similarly, H84T-BanLec exhibited potent antiviral activity against other human-pathogenic coronaviruses with dose-dependent reduction of mean viral RNA loads of 5.86-$\log_{10}$copies/ml, 3.55-$\log_{10}$copies/ml, and 2.87-$\log_{10}$copies/ml for SARS-CoV, HCoV-OC43, and HCoV-229E, respectively, at 90nM of H84T-BanLec (**Fig. 1g**). At ≥10nM, H84T-BanLec completely inhibited infectious SARS-CoV plaque formation with an EC_{50} of 6.02nM (**Extended Data Fig. 2a**). CPE was minimally observed in cells with ≥10.00nM (SARS-CoV) and ≥30.00nM (HCoV-229E) of H84T-BanLec (**Extended Data Fig. 2b**). Importantly, H84T-BanLec was similarly active against various emerging SARS-CoV-2 variants, including the B.1.1.7 (**Extended Data Fig. 3a**) and P.3 (**Extended Data Fig. 3b**) variants with EC_{50} at low nanomolar concentrations. No resistant mutant was detected after five serial passages of MERS-CoV and SARS-CoV-2 with H84T-BanLec in VeroE6 cells. These findings highlighted the pan-coronaviral antiviral activity and lack of resistance of H84T-BanLec against epidemic and circulating human-pathogenic coronaviruses, as well as emerging SARS-CoV-2 variants.

Potent *ex vivo* and *in vivo* activity of H84T-BanLec against MERS-CoV

High MERS-CoV RNA load and abundant viral nucleocapsid protein expression were detected in DMSO-treated *ex vivo* human lung tissue[22,23]. Treatment with 5-20nM of H84T-BanLec significantly (P<0.01) reduced MERS-CoV RNA load in a dose-dependent manner (**Fig. 2a**) and there was minimal viral nucleocapsid protein expression detected in human lung tissue explant treated with 20nM of H84T-BanLec (**Fig. 2b**). Next, we assessed the effect of H84T-BanLec in a human dipeptidyl peptidase 4 (hDPP4)-transgenic mouse model for MERS-CoV infection[23,24]. Intraperitoneal administration of H84T-BanLec resulted in significantly higher survival (80% vs 0%, P<0.05) (**Fig. 2c**) and less body weight loss (**Fig. 2d**) than the control mice receiving PBS. The mean viral RNA load (P<0.05) (**Fig. 2e**) and infectious virus titre (P<0.01) (**Fig. 2f**) were significantly reduced in the H84T-treated mice. The PBS-treated control mouse lung sections showed evidence of interstitial pneumonia, with peribronchiolar inflammatory infiltrates and thickened alveolar walls that were absent in the H84T-BanLec-treated mice (**Fig. 2g**). Immunofluorescence staining of the PBS-treated mouse lung sections showed abundant MERS-CoV nucleocapsid protein expression (green) while scarce viral nucleocapsid protein expression was observed in the lung sections of the H84T-treated mice (**Fig. 2h**). Together, these *ex vivo* and *in vivo* findings demonstrated the potent anti-MERS-CoV activity of H84T-BanLec.

Prophylactic and therapeutic effects of systemic and intranasal H84T-BanLec against SARS-CoV-2 in golden Syrian hamsters

To thoroughly characterize the *in vivo* prophylactic and therapeutic effects of H84T-BanLec administered by different routes against the pandemic SARS-CoV-2 in our established golden Syrian hamster model[25], we dosed the animals with either intraperitoneal or intranasal H84T-BanLec, with the first dose started 6 hours before or 24 hours after virus challenge. The hamsters that received either pre-challenge prophylactic or post-challenge therapeutic intraperitoneal H84T-BanLec had significantly lower viral RNA loads (**Fig. 3a**) and infectious virus titres (**Fig. 3b**) in the respiratory tract, as well as significantly lower

clinical scores (**Fig. 3c**) and less body weight loss (**Fig. 3d**) than did the PBS-treated control hamsters. Either pre-challenge prophylactic or post-challenge therapeutic H84T-BanLec resulted in near-complete protection from lung damage except for small focal areas of mild peribronchiolar and perivascular inflammatory infiltrates (**Fig. 3e**) and scarce SARS-CoV-2 nucleocapsid protein expression (**Fig. 3f**) as compared PBS-treated control hamsters. Importantly, the hamsters that received either pre-challenge prophylactic or post-challenge therapeutic intranasal H84T-BanLec also demonstrated significantly improved virological (**Figs. 3g and 3h**), clinical (**Figs. 3i and 3j**), and histopathological (**Figs. 3k and 3l**) parameters when compared to the PBS-treated control hamsters. While both prophylactic and therapeutic H84T-BanLec significantly ameliorated SARS-CoV-2 infection in the hamsters, prophylactic administration conferred higher protection than therapeutic administration with generally lower viral burden and clinical scores, as well as less histopathological change. These findings demonstrated the potential of both systemic and intranasal H84T-BanLec as effective prophylactic and therapeutic anti-SARS-CoV-2 options.

Effects on viral replication cycle and H84T-BanLec/SARS-CoV-2 spike co-localization in COVID-19 patient's lungs

To determine the steps of the SARS-CoV-2 replication cycle targeted by H84T-BanLec, we performed a time-of-drug-addition assay in a single replication cycle[26]. Pre-incubation of H84T-BanLec with VeroE6 cells did not inhibit SARS-CoV-2 replication (ie: -1h to 0h), indicating the absence of host receptor blockage. Similarly, maintenance of H84T-BanLec in the post-virus-entry stage (ie: 1h to 8h) did not decrease intracellular viral load. In contrast, either mixing SARS-CoV-2 with H84T-BanLec pre-infection or adding H84T-BanLec during virus absorption (ie: 0h to 1h) significantly reduced viral load ($P<0.01$), indicating that H84T-BanLec interfered with SARS-CoV-2 entry (**Extended Data Fig. 4**). These findings are compatible with one of the potentially expected mechanisms of action of BanLec, which has been found to inhibit the replication of other RNA viruses by binding to the high-mannose glycans found on viral proteins and inhibiting virus entry[2,19-21]. For coronaviruses, the highly glycosylated spike protein, which mediates virus entry with host cells, is the likely target of H84T-BanLec. To validate the interaction between H84T-BanLec and SARS-CoV-2 spike protein in human, we performed co-localization experiments using the autopsied lung sections of a deceased COVID-19 patient. As shown in **Extended Data Fig. 5**, H84T-BanLec indeed co-localized with the majority of the SARS-CoV-2 spike proteins found in the autopsied human lung tissue.

Real-time structural analysis of H84T-BanLec/SARS-CoV-2 spike binding interactions

To understand the binding interactions between H84T-BanLec and the SARS-CoV-2 spike at the atomic and molecular level, we first applied high-speed atomic force microscopy (HS-AFM) to visualize the isolated SARS-CoV-2 full-length spike protein and its highly dynamic movements[27,28]. Snapshots captured from a HS-AFM movie revealed that three arms are waggling around a central core, in accordance with a 3-dimensional crystal structure in which three monomeric units of the S protein are entangled to form a trimeric assembly (**Fig. 4a**). We also mapped isolated H84T-BanLec molecules to identify different oligomers and measured their respective mean volumes using AFM scans, which

showed that our preparation contained 29% monomers (343±73nm^3), 50% dimers (604±71nm³), and 21% tetramers (1190±85nm^3). This finding elucidates previous disagreements as to whether H84T-BanLec exist primarily as a dimer or as a tetramer[2,29]. The topographical images matched well with 3D structures of each oligomeric state (**Fig. 4b**). Next, we employed AFM-derived single-molecule force spectroscopy (SMFS) to directly measure the dissociation forces between H84T-BanLec and the full-length SARS-CoV-2 spike protein by mechanically pulling on bonds formed by molecular recognition from the two cognate molecules (**Fig. 4c**)[30,31]. The SARS-CoV-2 spike trimer was conjugated to the AFM tip via a 6nm-long flexible PEG linker to ensure sufficient motional freedom for unconstrained specific binding. Consecutive force-distance (F-D) measurement cycles, during which an AFM tip carrying the SARS-CoV-2 spike was brought into contact with a dense layer of H84T-BanLec molecules immobilized to a surface to allow H84T-BanLec/SARS-CoV-2 spike bonds to form, were performed. Thereafter, the AFM cantilever tip was retracted to measure the unbinding forces required to break the bonds. A typical F-D cycle initially shows nonlinear stretching behaviour resulting from the flexibility of the PEG linker, then finally bond breakage occurred at a critical unbinding force (**Fig. 4d**). The detected forces were used to construct the experimental probability density functions (PDFs) of unbinding forces resulting in dissociation of the H84T-BanLec/SARS-CoV-2 spike bond (**Fig. 4e**). A characteristic force distribution recorded when the spike-adorned AFM tip was allowed to rest for 10ms on the surface containing H84T-BanLec (dwell time) shows a bimodal distribution, with the main peak at about 50pN and a second peak at about 110pN. The first and the second peaks represent the simultaneous rupture of 1 and 2 H84T-BanLec/SARS-CoV-2 spike bonds, respectively. Increasing the dwell time enhances the probability of multiple bond formation, as evidenced by the multimodal force histogram recorded at a dwell time of 100ms, which verifies simultaneous unbinding of 1, 2, and 3 H84T-BanLec molecules from one homotrimeric SARS-CoV-2 spike[31]. Additionally, we observed sequential bond rupture behaviours in our F-D curves arising from the breaking of up to 4 bonds (**Fig. 4f**). These results indicated that up to 4 H84T-BanLec molecules may bind to each SARS-CoV-2 spike trimer.

To decipher the dynamic features of the H84T-BanLec/SARS-CoV-2 spike bonds, we extended our SMFS studies to dynamic force spectroscopy (DFS) experiments and varied the pulling speed. Individual dissociation forces were plotted versus their force loading rate (pulling speed times effective spring constants of molecules and AFM cantilever). H84T-BanLec/SARS-CoV-2 spike interaction forces arising from single bond breakages (red dots, **Fig. 4g**) were well fitted by the widely used Bell-Evans model (red line, **Fig. 4g**)[32,33], yielding a kinetic dissociation rate constant of k_{off} =0.046±0.02s^{-1}. The kinetic on-rate constant (k_{on}), approximated from computing the binding probability P(t) as a function of the dwell time t[31,34], according to $P=A(1-\exp(-(t-t_o)/\tau))$, and calculated using $k_{on}=1/\tau*C_{eff}$ (effective concentration of molecules coupled to the AFM tip), yielded k_{on}=9.98±5.18×10^4 (1/Ms). The equilibrium dissociation constant (K_D), determined from the kinetic rate constants ($K_D=k_{off}/k_{on}$), was 0.46μM. In addition, spontaneous thermodynamic association and dissociation was measured with surface plasmon resonance (SPR)[35]. H84T-BanLec was injected at different concentrations into chambers containing either the isolated SARS-CoV-2 spike-receptor-binding domain (RBD) or complete SARS-CoV-2 spike

trimers coupled to chip surfaces and subsequently removed with buffer. The SARS-CoV-2 spike-RBD alone failed to bind to H84T-BanLec (**Extended Data Fig. 6**). For the SARS-CoV-2 spike trimer, experimental binding curves (coloured lines, **Fig. 4h**) recorded with SPR were fitted with the "bivalent analyte model" (black lines, **Fig. 4h**), which assumes two-step binding of H84T-BanLec to adjacent immobilized spike trimer binding sites. A very good match of the fit with the data confirms that H84T-BanLec is mainly present in its dimeric form (**Fig. 5a**). Kinetic rates and the K_D value determined from spontaneous thermodynamic association and dissociation with SPR were similar to those from force-probing in DFS (**Supplementary Table S1**), providing a consistent picture for the dynamics and equilibrium of H84T-BanLec/SARS-CoV-2 spike interactions.

Interaction dynamics and structural flexibility of H84T-BanLec/SARS-CoV-2 spike complex binding sites

To depict the dynamics of the H84T-BanLec/SARS-CoV-2 spike interactions, we filmed the complexes using real-time HS-AFM under physiological conditions (**Supplementary Video S1**). H84T-BanLec interacted with SARS-CoV-2 spike at the periphery around the core of the trimeric structure (**Fig. 5a**). A sequence of 30 frames from movie recordings of H84T-BanLec/SARS-CoV-2 spike complexes that showed continuous association and dissociation was selected to quantify the complex volume in each of the frames. By comparing the volumes of the complexes with that of H84T-BanLec dimers and isolated SARS-CoV-2 spike trimers, we found that on average each SARS-CoV-2 spike trimer bound to 4.1±0.7 H84T-BanLec dimers. Volume distributions showed that 46% of the SARS-CoV-2 spike trimers bound to about 4 dimers each (**Fig. 5b**). A similar number of multimeric interactions were also observed in SMFS traces, as evident from the sequential bond breakages (**Fig. 5c**). From these recordings, we determined the distances between the ruptures and constructed an experimental PDF. The PDF distribution of the rupture distances revealed 3 distinct peaks with maxima located at 3.8nm, 10.1nm, and 21.1nm, respectively (**Fig. 5d**). These findings indicated that a H84T-BanLec dimer can bind to several binding sites at distinct distances on the surface of the SARS-CoV-2 spike trimer.

The N234 glycosylation site is the only site that exclusively carries up to 9 mannose residues on the SARS-CoV-2 spike, and this specific amino acid has been suggested to control the ability of spike to assume the proper conformation for binding to ACE2[36]. To depict the multimeric interaction pattern, we modelled the 9-mannose site at N234 as well as the 5-mannose sites according to the data of Watanabe et al[37], and calculated possible distances between the high-mannose residues. Note that the glycan at N164 was identified by Watanabe et al. as almost exclusively of complex type, while Zhao et al. assigned about 15% of oligomannosidic glycans to this site[38]. Analyses on our own samples suggested up to 29% of oligomannosidic glycans at N165[39], such that we have included this site in our analysis. Distinct multiple binding paths along oligo (5)-mannose glycan sites within the SARS-CoV-2 spike trimer are shown with orange lines in the 3-dimensional model structure, indicating 3.2nm to the glycan at N61, 4.3nm for the glycan at N165, and 10-12nm for adjacent monomers of spike, or for glycans at the stalk (N709 and N1074) (**Fig. 5e**). Indeed, the estimated distances between oligo-mannose glycans in the 3-dimensional model are in agreement with distances derived from SMFS bond dissociation ruptures.

Consistent with the position of the first peak at 3.8nm, the short path correlates with a distance between the 9-mannose site N234 and a 5-mannose site at N61 or at N165. Similar calculations for other paths, such as from N234 to another 5-mannose site or across the spike monomer correlated with the second peak of the length distribution at 10.1 nm, which might be slightly influenced by mechanical twists along the pulling direction in SMFS experiments. The length distributions of H84T-BanLec/SARS-CoV-2 spike dissociation revealed multimeric interactions between the H84T-BanLec dimer and different glycosylation sites on the SARS-CoV-2 spike. This was further evidenced by the 3-dimensional AFM topographical time frames, which provided direct visualization of the formation of bonds to various SARS-CoV-2 spike high-mannose sites in real-time (**Fig. 5f**). To directly test whether N234 is crucial to the interaction between H84T-BanLec and the spike protein, we examined whether H84T-BanLec could bind as effectively to spike with a mutation at position N234 as it does to wild-type spike. The binding affinity of the N234Q mutant to H84T-BanLec was determined with SPR measurements (**Extended Data Fig. 6a & Supplementary Table S1**). Interestingly, H84T-BanLec even binds slightly more favourably to the N234Q mutant than to the wild-type spike with a slightly higher k_{on} value and a significantly lower k_{off} rate, as well as a higher binding saturation. We conclude that H84T-BanLec does not exclusively bind to the high-mannose glycan at N234, but that binding to the other indicated oligomannosidic glycans is as relevant, in agreement with our analyses of the interglycan distances.

Discussion

Novel coronaviruses have and will likely continue to emerge as important human pathogens. As evidenced by the ongoing COVID-19 pandemic, the traditional “one virus, one drug” antiviral discovery strategy is inefficient for the control of rapidly disseminating outbreaks. Broad-spectrum drug compounds with “pan-coronaviral” activities that target conserved viral components utilized by all coronaviruses for replication, such as the spike, are urgently needed for the current and future coronavirus pandemics. Lectins such as BanLec, griffithsin, and Flt3 Receptor Interacting Lectin (FRIL) bind to carbohydrates to exert broad-spectrum antiviral activities, but have not advanced into clinical use as antivirals, in part due to their potential mitogenicities (save griffithsin)[2,40,41]. To overcome this bottleneck, we have previously engineered the H84T-BanLec, which exhibits broad-spectrum antiviral activities with significantly reduced mitogenicity and broad-spectrum antiviral activities against all influenza viruses tested[2,20,21]. Further, it is highly effective *in vivo* against influenza whether given intranasally or systemically[2,20].

In this study, we report the pan-coronaviral activities of H84T-BanLec against known human-pathogenic coronaviruses, including the highly virulent MERS-CoV (overall mortality rate >30%), the pandemic SARS-CoV-2, the 2003 SARS-CoV, and other circulating HCoVs. The potent antiviral activity of H84T-BanLec against MERS-CoV was well evident in the *ex vivo* human lung organ tissue culture and human DPP4-transgenic mouse models. Moreover, by administering H84T-BanLec via different routes and starting at different times in relation to virus challenge, we showed that this broad-spectrum lectin is highly effective against SARS-CoV-2 as an intranasal or systemic prophylaxis or therapy. For the control of pandemics caused by highly transmissible viruses like SARS-CoV-2, which causes mild or even asymptomatic

infection in a significant proportion of patients, it is especially important to develop effective prophylactic and therapeutic agents that can be administered topically (intranasally) in the outpatient setting to reduce the burden on healthcare facilities and quarantine camps. Importantly, our current study confirms that H84T-BanLec primarily exists as a dimer, which makes it highly stable and thus ideally suitable for development as a topical agent[2]. H84T-BanLec also holds promise for systemic use, as it has a very long half-life (>35 hours), so it likely would have to be administered only one time in the outpatient and inpatient settings[20,21]. The total amount of protein required would be similar to that of monoclonal anti-SARS-CoV-2 antibodies[16,20,21], and systemic H84T-BanLec is very well tolerated in mice, hamsters, and rats (unpublished data)[20]. Unlike monoclonal antibodies, to which resistant viral mutants might be expected to develop, the high number of available binding sites of high-mannose glycans on spikes of coronaviruses will render resistance to H84T-BanLec much less likely.

Regarding H84T-BanLec's anti-coronaviral mechanism of action, we demonstrated that H84T-BanLec binds to the glycosylated spike protein in the lung tissues of a deceased COVID-19 patient. Time-of-drug-addition studies showed that virus entry into cells is a major step in the SARS-CoV-2 replication cycle that is perturbed by the lectin. Corroboratively, our experiments found that H84T-BanLec can compete for binding between the ACE2 cellular receptor and the spike protein (**Extended Data Fig. 7**), thus inhibiting virus entry. Extensive structural and biophysical studies using HS-AFM and SMFS demonstrate the interaction dynamics and binding capability between H84T-BanLec and SARS-CoV-2 spike. As the SARS-CoV-2 spike is quite flexible, strong and diverse bonds would be necessary for maximal binding with H84T-BanLec and the resulting antiviral effects. Our data demonstrated the presence of strong interactions with formation of multiple bonds between H84T-BanLec and SARS-CoV-2 spike, and that these bonds can also form across two distinct spike monomers. While N234 is decorated with 9-mannose molecules and has been suggested to control the position of the RBD[36], our data showed that this is not the only site on spike recognized by H84T-BanLec. In fact, modelling and experimental data suggested a network of oligomannosidic glycans to which H84T-BanLec binds. However, H84T-BanLec does not bind to the isolated RBD, in agreement with the fact that no mannosidic glycans were determined on the RBD. An intriguing glycosylation site is found at position N165. Not all experimental glycan analyses identified this glycan as oligomannosidic, but it is placed right next to the RBD and binding of H84T-BanLec to it can be expected to directly affect the orientation of the RBD and the interaction between the RBD and ACE2. These structural data are essential for further compound optimization and analogue development.

In summary, the present study reports the broad-spectrum and potent activity of H84T-BanLec against a broad range of human-pathogenic coronaviruses. The promising *in vivo* data and structural analysis demonstrating the high stability of H84T-BanLec and its strong binding interactions with SARS-CoV-2 spike highlight its potential to be applied clinically as both an intranasal and systemic agent for the ongoing COVID-19 pandemic and future coronavirus outbreaks.

Materials And Methods

Chemicals, viruses, and cells

H84T-BanLec was prepared as previously described[2]. MERS-CoV (EMC/2012) was kindly provided by Ron Fouchier (Erasmus Medical Center, the Netherlands)[4]. SARS-CoV-2 (HKU-001a strain, and the B.1.1.7 and P.3 variants) were isolated from the respiratory tract specimens of COVID-19 patients in Hong Kong. Archived clinical strains of SARS-CoV, HCoV-OC43, and HCoV-229E were obtained from the Department of Microbiology, The University of Hong Kong (HKU). The cell lines used in this study were available in our laboratory as previously described[42-44]. All experimental protocols involving live MERS-CoV, SARS-CoV-2, and SARS-CoV followed the approved standard operating procedures of HKU Biosafety Level 3 facility.

Cytotoxicity and antiviral assays

The cytotoxicity of H84T-BanLec in various cell lines was determined using the CellTiter-Glo® luminescent cell viability assay (Promega Corporation, Madison, WI) according to manufacturer's instructions and as previously described[24,45]. Viral load reduction, CPE inhibition, and plaque reduction assays for coronaviruses were performed as we previously described[46,47]. To test the vulnerability of H84T-BanLec to induce resistant escape mutants, a drug resistance assay was performed as we described previously[48]. In brief, MERS-CoV and SARS-CoV-2 (MOI=0.01) was passed in the presence of about 5× EC_{50} of H84T-BanLec (30nM) for 8 passages and in VeroE6 cells. After the 8 passage, the antiviral activities of HB84T-BanLec against the wild-type and passaged viruses were compared using viral load reduction assay.

Ex vivo human lung tissue organ culture

The anti-MERS-CoV activity of H84T-BanLec was evaluated in an established *ex vivo* human lung tissue organ culture model as we described previously[22,23]. The human lung tissues were obtained from patients with lung tumours who underwent surgical operations at Queen Mary Hospital, Hong Kong. Briefly, the freshly isolated human lung tissues were rinsed with the primary tissue culture medium, which contained the advanced Dulbecco's Modified Eagle Medium (DMEM)/F12 medium supplemented with 2mM HEPES (Gibco, Thermo Fisher Scientific, Waltham, MA, USA), 1×GlutaMAX (Gibco), 100U/ml penicillin, 100μg/ml streptomycin, 20μg/ml vancomycin, 20μg/ml ciprofloxacin, 50μg/ml amikacin, and 50μg/ml nystatin. Human lung tissues were cut into small pieces at comparable sizes and then infected with MERS-CoV at 1×10^6 plaque-forming units (PFU)/ml in a 6-well culture plate. After 2h, the inoculum was removed and the specimens were washed with the primary tissue culture medium. The infected specimens were then transferred to inserts of 12-well transwells (Corning Life Sciences, Tewksbury, MA, USA) pre-coated with 200μl 60% Matrigel (Corning Life Sciences) diluted with the primary tissue culture medium. An additional 60% Matrigel was then added to the insert to seal the explant. The basolateral compartment was filled with 1ml of the primary tissue culture medium supplemented with 0, 5, or 20μM H84T-BanLec. The samples were harvested at 24hpi for confocal microscopy and qRT-PCR analysis. The virus genome copies in cell lysate samples were normalized with GAPDH copy numbers.

Immunofluorescence staining of MERS-CoV nucleocapsid protein in the lung tissues was performed as previously described[22,49,50].

Co-localization of H84T-BanLec and SARS-CoV-2 proteins in autopsied lung sections

Autopsied lung sections of a deceased COVID-19 patient were obtained from the Department of Pathology, University of Michigan[51] and sequentially stained with biotinylated H84T-BanLec (1:25k, Opal 620 reporter), and antibodies to SARS-CoV-2 nucleocapsid (Genetex, GTX635679, 1:1000, Opal 570 Reporter) and spike proteins (Genetex, GTX632604, 1:50, Opal 690 Reporter). After each round of antigen detection, the slides were exposed to microwave epitope retrieval in 10mM citrate buffer to remove the antibody complex, leaving behind the deposited fluorochrome. The slide was then imaged. A pseudo-coloured image was created. Original monochrome images were analyzed using the coloc 2 sub-routine in FIJI and the Pearson correlation coefficient was calculated[52].

hDPP4-transgenic mouse model for MERS-CoV infection

The *in vivo* anti-MERS-CoV activity of H84T-BanLec was evaluated in an established hDPP4-transgenic mouse model as we described previously[23,24]. Briefly, hDPP4 mice, aged 5-8 weeks, were obtained from the HKU Centre for Comparative Medicine Research and divided into different groups to receive H84T-BanLec or sham (PBS) treatment. After anaesthesia, the mice were intranasally inoculated with 20μl of virus suspension containing 500PFU of MERS-CoV (n=10 per group). Each mouse in the H84T-BanLec group was treated with intraperitoneal (15 mg/kg/animal/day every 24h) H84T-BanLec starting at 6 hours before virus challenge until 3dpi. The control mice were treated with intraperitoneal PBS starting at 6h before virus challenge daily until 3dpi. Five animals per group were sacrificed at 4dpi for viral load quantitation by qRT-PCR, virus titer quantitation by plaque assay, and histopathological studies as described previously[23, 24]. The survival rates and body weight changes of the remaining 5 animals per group were observed until 14dpi or death as described previously. Immunofluorescence staining for MERS-CoV nucleocapsid protein expression was performed as we described previously[24].

Golden Syrian hamster model for SARS-CoV-2 infection

The *in vivo* anti-SARS-CoV-2 activity of H84T-BanLec was evaluated in an established golden Syrian hamster as we described previously[25,45]. Briefly, male and female golden Syrian hamsters, aged 6-10 weeks, were obtained from the Chinese University of Hong Kong Laboratory Animal Service Centre through the HKU Centre for Comparative Medicine Research. The hamsters were divided into different groups to receive H84T-BanLec or sham (PBS) treatment and their clinical scores were recorded as described previously[53]. At 0dpi, each hamster was intranasally inoculated with 100μL of DMEM containing 10^5 PFU of SARS-CoV-2 (HKU-001a strain) under intraperitoneal ketamine (200mg/kg) and xylazine (10mg/kg) anaesthesia. The H84-BanLec group hamsters were treated with intraperitoneal (15.0mg/kg/day every 24h) or intranasal (1.5 mg/kg/animal/day every 24h) H84T-BanLec starting at 6h before virus challenge (pre-challenge) or 24h after virus challenge (post-challenge) until 3dpi (n=10 per

group). The control hamsters were treated with intraperitoneal or intranasal PBS starting at 6h before virus challenge daily until 3dpi (n=10 per group). Five animals per group were sacrificed at 4dpi for viral load quantitation by qRT-PCR, virus titer quantitation by plaque assay, and histopathological studies as described previously[13]. The survival rates and body weight changes of the remaining 5 animals per group were observed until 14dpi or death. Immunofluorescence staining for SARS-CoV-2 nucleocapsid protein expression was performed as we described previously[13].

Time-of-drug-addition assay

Time-of-drug-addition assay was performed as we described previously to determine the phase(s) of the SARS-CoV-2 replication cycle targeted by H84T-BanLec[26]. Briefly, VeroE6 cells were infected with SARS-CoV-2 (MOI=3.0) and 20nM H84T-BanLec was added pre-infection (-1h), at the time of infection (0h), pre-incubated with SARS-CoV-2 pre-infection, or at 1h post-infection. Intracellular viral genome copy numbers of the corresponding time points were determined at 8h post-infection by qRT-PCR and compared with PBS-treated controls.

Ethical approvals

The *ex vivo* human lung tissue culture experiments and the animal experiments were approved by the Institutional Review Board of HKU/Hospital Authority Hong Kong West Cluster and the HKU Committee on the Use of Live Animals in Teaching and Research, respectively. The autopsy of the deceased COVID-19 patient was exempt from institutional review board approval.

Statistical analysis

All data were analysed with GraphPad Prism software (GraphPad Software, Inc). One-way ANOVA or student's t-test was used to determine significant differences in viral loads and titers, and Kaplan-Meier survival curves were analysed by the log rank test. $P<0.05$ was considered statistically significant.

Conjugation of SARS-CoV-2 spike trimer and H84T-BanLec through histidine residues of His-tagged protein

A maleimide-Poly(ethylene glycol) (PEG) linker was attached to a 3-aminopropyltriethoxysilane (APTES)-coated AFM cantilever (or silicon nitride surface for H84T-BanLec immobilization) by incubating the cantilevers for 2h in 500µL of chloroform containing 1mg of maleimide-PEG-N-hydroxysuccinimide (NHS) (Polypure, Oslo, Norway) and 30µl of triethylamine. After washing 3 times with chloroform and drying with nitrogen gas, the cantilevers were immersed for 2h in a mixture of 100µL of 2mM thiol-trisNTA, 2µL of 100mM EDTA (pH 7.5), 5µL of 1M HEPES (pH 7.5), 2µl of 100mM tris(carboxyethyl)phosphine (TCEP) hydrochloride, and 2.5µL of 1M HEPES (pH 9.6) buffer, and subsequently washed with HEPES-buffer saline (HBS). Thereafter, the cantilevers were incubated for 4h in a mixture of 4µL of 5mM $NiCl_2$ and 100µL of 0.2µM His-tagged Spike trimer. After washing with HBS, the cantilevers were stored in HBS at 4°C[54].

Single-Molecule Force Spectroscopy (SMFS) measurement

Force distance measurements were performed at room temperature (~25ºC) using cantilevers with 0.01N/m nominal spring constants (MSCT, Bruker) in TBS buffer containing 1mM $CaCl_2$, and 0.1% Tween-20. Precise spring constant values of AFM cantilevers were determined by measuring the thermally driven mean-square bending of the cantilever using the equipartition theorem in an ambient environment[55]. The deflection sensitivity was calculated from the slope of the force-distance curves recorded on a bare silicon substrate. Determined spring constants ranged from 0.008-0.015N/m. Force-distance curves were acquired by recording at least 1000 curves with vertical sweep rates between 0.5s and 10s and at a z-range of typically 500-1000nm, resulting in a loading rate from 10-10,000pN/s, using a commercial AFM (Keysight Technologies, USA). The relationship between experimentally measured unbinding forces and parameters depicting the interaction potential were deciphered using the kinetic models of Bell, and Evans and Ritchie[32,33].

Length data analysis

Software for data analysis was written in Matlab (MathWorks, Inc.). Force curves (n=4000, 2 different tips) were analysed for the calculation of the distance and for the construction of experimental probability density function (PDF) of distance. The distance between two unbinding events was calculated with the correction of the cantilever deflection. Thereafter, for each length difference and the corresponding standard deviation given by the pixel mash of the data recordings, single Gaussians with unitary area were constructed, summed up, and normalized to calculate the experimental probability density function. This data presentation is advantageous over conventional histograms, as the data accuracy is taken into account and binning artefacts can be avoided.

Surface Plasmon Resonance (SPR) measurement

SPR was used to study the kinetics of binding and dissociation of H84T-BanLec to SARS-CoV-2 spike protein in real time. SARS-CoV-2 spike protein was immobilized onto a Sensor Chip NTA (cytiva) via its His_6-tag after washing the chip for at least 3min with 350mM EDTA and activation by applying a solution of 0.5mM $NiCl_2$ for 1min. 50nM SARS-CoV-2 spike protein was injected multiple times to generate a stable surface. For the determination of kinetic and equilibrium constants, H84T-BanLec was injected at different concentrations (10-200nM) and subsequently removed with buffer. Running buffer was TBS, pH 7.4, containing 0.1% Tween-20, 1% BSA, and 1mM Ca^{2+}. The resulting experimental binding curves were fitted using the “bivalent analyte model”, assuming two-step binding of H84T-BanLec to SARS-CoV-2 spike protein.

Cell culture experiments

Inhibition measurements

All force-distance curves were recorded at room temperature by using a PicoPlus 5500 AFM setup (Agilent Technologies, Chandler, AZ, USA) on living cells with the assistance of a CCD camera for localization of the cantilever tip on selected cells. The optical system of the AFM was focused on the cantilever tip, while the sample plate with the Petri dish was moved upwards by the step motor. Before the cells on the dish reached the focus, the piezo tube of the AFM was started to scan in the z-axis with a scanning range of 3μm and at a scanning frequency of 1Hz. The sample plate was moved upwards by the step motor using manual control with 1μm per step. Due to the resistance of the liquid, a gap between the approaching curve and the retraction curve appeared, when the AFM tip was close to the sample surface. About 2μm before the AFM tip touched the sample surface, the approaching curve was no longer parallel to the retraction curve. With this signal, the movement of the step motor was stopped. Further approaching was accomplished by gradually changing the voltage on the piezo tube. With this approaching method, the indentation force of the first contact between the AFM tip and the sample surface was controlled to be less than 30pN.

The functionalized cantilever (pegylated with SARS-CoV-2 spike protein) with a nominal spring constant of 0.01N/m was moved downward to the cell surface and moved upward after the deflection of the cantilever reached the force limit. The deflection (*z*) of the cantilever was monitored by a laser beam on the cantilever surface and plotted *versus* the Z-position of the scanner, from which the force (*F*) was determined according to Hook's law ($F = kz$, with k being the cantilever spring constant). When the tip tethered molecule bound to ACE2 on the cell surface, a pulling force developed during the upward movement of the cantilever causing the cantilever to bend downwards. At a critical force, i.e. the unbinding force, the tip tethered spike protein detached from ACE2, and the cantilever jumped back to its neutral position. The sweep range was fixed at 3000nm and the sweep rate was set at 1 Hz. On each cell, at least 100 force-distance cycles with 2000 data points per cycle and typical force limit of about 30pN were recorded.

Structural data analysis

The unbinding event was identified by local maximum analysis using a signal-to-noise threshold of 2. The binding activity was calculated from the fraction of curves showing unbinding events. Two-tailed Student's t-test was performed for statistical analysis.

High-speed atomic force microscopy (HS-AFM) imaging

10nM of purified SARS-CoV-2 spike protein was suspended in imaging buffer (10mM Hepes, pH 7.4, 140mM NaCl, 5mM KCl, 1mM CaCl, 1mM MgCl), containing 5μM $NiCl_2$, of which 1.5μL were applied to freshly cleaved mica disc (2mm diameter). After 3min, the surface was rinsed with ~15μL imaging buffer (without drying) and the sample was mounted in the imaging chamber of the HS-AFM (RIBM, Japan). Similarly, H84T-BanLec stock was diluted to 2μM in imaging buffer and 1.5μL of the diluted solution was applied to mica for 3 min, rinsed with 15μL imaging buffer, and imaged using HS-AFM. For following the complexation of H84T-BanLec and SARS-CoV-2 spike protein, the SARS-CoV-2 spike trimer was deposited

on mic as descrbed above, before 2μM H84T-BanLec was added to the imaging chamber. For imaging, we used ultra-short cantilevers USC-F1.2-k0.15 (NanoWorld) with nominal spring constant 0.15N/m, resonance frequency of ~500kHz, and quality factor of ~2. During image acquisition, the amplitude was set to 85-90% of the free amplitude (~3nm) and kept constant using a feedback loop.

HS-AFM image processing and volume measurement

Horizontal scars, which occurred due to feedback instabilities or particles sticking to the AFM tip, were selected and removed by Laplacian background substitution. A height threshold mask was used for selecting the background prior to correction of scanning artefacts. Next, Gaussian filter was applied to the images. For the volume measurement, the protein surface was selected using a height threshold mask defined from a minimum height of 0.25-0.35nm to the maximum height of the protein structure. Image processing was done using Gwyddion 2.55.

Three-dimensional structural modelling

All structural models of the SARS-CoV-2 spike trimer were made from the fully glycosylated 3D model of the SARS-CoV-2 spike trimer, based on the cryo-EM structure of Walls et al. (PDB: 6VYB)[56]. Curved distances over the surface of the protein between glycans were calculated using the distance field algorithm[57]. This algorithm determines the shortest distance between the centres of geometry of selected glycans over a grid with grid-spacing of 0.5nm, avoiding any grid points that are within 0.5nm of any protein atom. The path was further smoothened by averaging over 5 neighbouring path points. Models of the complex of spike with H84T-BanLec were created using the structure of BanLec (PDB: 4PIK)[2]. A superposition of the bound carbohydrates of chain A of this model with the oligomannosidic glycan at N234 of the SARS-CoV-2 spike was performed to create models of the H84TBanLec/SARS-CoV-2 spike complex.

Declarations

Acknowledgments

This study was partly supported by funding to The University of Hong Kong: the Health and Medical Research Fund (COVID190121 and 15140762), the Food and Health Bureau, The Government of the Hong Kong Special Administrative Region; Innovation and Technology Fund (ITF), the Government of the Hong Kong Special Administrative Region; the Consultancy Service for Enhancing Laboratory Surveillance of Emerging Infectious Diseases and Research Capability on Antimicrobial Resistance for Department of Health of the Hong Kong Special Administrative Region Government; the National Program on Key Research Project of China (grant no. 2020YFA0707500 and 2020YFA0707504); Sanming Project of Medicine in Shenzhen, China (SZSM201911014); the High Level-Hospital Program, Health Commission of Guangdong Province, China; and the Major Science and Technology Program of Hainan Province (ZDKJ202003); and donations from the Shaw Foundation of Hong Kong, the Richard Yu and Carol Yu, Michael Seak-Kan Tong, May Tam Mak Mei Yin, Lee Wan Keung Charity Foundation Limited, Hong Kong

Sanatorium & Hospital, Hui Ming, Hui Hoy and Chow Sin Lan Charity Fund Limited, Chan Yin Chuen Memorial Charitable Foundation, Marina Man-Wai Lee, the Hong Kong Hainan Commercial Association South China Microbiology Research Fund, the Jessie & George Ho Charitable Foundation, Perfect Shape Medical Limited, Kai Chong Tong, Tse Kam Ming Laurence, Foo Oi Foundation Limited, Betty Hing-Chu Lee, Ping Cham So, and Lo Ying Shek Chi Wai Foundation. This work was supported by the grants to D.M.M. from the Defense Threat Reduction Agency (HDTRA1-15-1-0067), the University of Michigan MTRAC (Michigan Translational Research and Commercialization Life Sciences), and the Forbes Institute of the University of Michigan Cancer Center. This work was supported by funding from the Austrian National Foundation for Research, Technology, and Development and Research Department of the State of Upper Austria (Y.O.), from the FWF projects V584 (Y.O.), P31599 (R.Z.), I3183(P.H.), the WWTF grant LS19-029 (P.H., D.C.), the ÖAW fellowship STIP13202002 (L.H.), and the European Union's Horizon research and innovation programme (H2020-MSCA-ITN-2016) under the Marie Skolodowska-Curie grant agreement No. 721874 (P.H., D.C.). D.T. acknowledges funding from the Department of Pathology, University of Michigan and Allecia Wilson and the Wayne County Medical Examiner's office for providing access to the autopsy material. J.M.P. has received funding from the T. von Zastrow foundation, the FWF Wittgenstein award (Z 271-B19), the Austrian Academy of Sciences, the Innovative Medicines Initiative 2 Joint Undertaking (JU) under grant agreement No 101005026, and the Canada 150 Research Chairs Program F18-01336 as well as the Canadian Institutes of Health Research COVID-19 grants F20-02343 and F20-02015. C.O. acknowledges funding by the Rapid Response program of the Vienna Science and Technology Fund (WWTF; grant no. COV20-015). The funding sources had no role in the study design, data collection, analysis, interpretation, or writing of the report.

Author contributions

J.F.-W.C., Y.O., S.Y. and H.C. contributed equally to this work. J.F.-W.C., Y.O., S.Y., H.C., P.H., K.Y.Y. and D.M.M. had roles in the study design, data collection, data analysis, data interpretation, literature search, and writing of the manuscript. J.F.-W.C., S.Y., H.C., M.-L.Y., C.C.-S.C., V.K.-M.P., C.C.-Y.C., A.J.Z., J.-P.C., L.W., K.K.-H.C., H.S., Y.W., Y.H., C.L., W.-M.C., K.K.-W.T. and K.-H.C. performed the *in vitro*, *ex vivo*, and/or animal experiments and analysed the data. Y.O. performed force spectroscopy measurements and analysed the data. D.C. performed HS-AFM measurements and analysed the data. M.L., K.-Y.S. and W.-K.A. provided critical reagents and/or tissues for the experiments. R.Z. performed AFM binding activity measurements and analysed the data. L.H. performed SPR measurement and analysed the data. D.G.T. performed the co-localization experiments using autopsied lung sections. M.K. produced the N234Q spike glycoprotein mutant. J.M.P. provided conceptual advice and troubleshooting. C.O. performed the molecular modeling experiments and visualized the H84T-BanLec and spike proteins. P.H., K.-Y.Y. and D.M.M. oversaw the conception and supervised the study. J.F.-W.C., K.-Y.Y. and D.M.M. provided funding support.

Competing interests

J.F.-W.C. has received travel grants from Pfizer Corporation Hong Kong and Astellas Pharma Hong Kong Corporation Limited and was an invited speaker for Gilead Sciences Hong Kong Limited and Luminex

Corporation. D.M.M. is an inventor on patents U.S. No. 8,865,867 “Lectins and Uses Thereof”; U.S. No. 9,481,717 “Lectins and Uses Thereof”; European No. 2558488 (DE, GB, FR) “Banana Lectins and Uses Thereof”; Chinese No. 103025756 “Banana Lectins and Uses Thereof”; and U.S. No. 10,450,355 “Lectins and Uses Thereof”. The other authors declare no competing interests.

Correspondence and requests for materials should be addressed to P.H., K.-Y.Y or D.M.M.

Data availability

Complete sequences of the SARS-CoV-2 strains are available through GenBank or GISAID [GenBank accession number: MT230904 (HKU-001a), GISAID accession number EPI_ISL_1273444 (B.1.1.7 variant) and GISAID accession number EPI_ISL_1660475 (P.3 variant)]. Other supporting raw data are available from the corresponding authors upon reasonable request. Source data are provided with this paper.

References

1. Chan, J.F., To, K.K., Tse, H., Jin, D.Y. & Yuen, K.Y. Interspecies transmission and emergence of novel viruses: lessons from bats and birds. *Trends Microbiol.* **21**, 544-555 (2013).
2. Swanson, M.D. et al. Engineering a therapeutic lectin by uncoupling mitogenicity from antiviral activity. *Cell*. **163**, 746-758 (2015).
3. Peiris, J.S. et al. Coronavirus as a possible cause of severe acute respiratory syndrome. *Lancet*. **361**, 1319-1325 (2003).
4. Zaki, A.M., van Boheemen, S., Bestebroer, T.M., Osterhaus, A.D. & Fouchier, R.A. Isolation of a novel coronavirus from a man with pneumonia in Saudi Arabia. *N. Eng. J. Med.* **367**, 1814-1820 (2012).
5. Zhou, P. et al. A pneumonia outbreak associated with a new coronavirus of probable bat origin. *Nature.* **579**, 270-273 (2020).
6. Chan, J.F. et al. A familial cluster of pneumonia associated with the 2019 novel coronavirus indicating person-to-person transmission: a study of a family cluster. *Lancet.* **395**,514-523 (2020).
7. Cheng, V.C., Lau, S.K., Woo, P.C. & Yuen, K.Y. Severe acute respiratory syndrome coronavirus as an agent of emerging and reemerging infection. *Clin. Microbiol. Rev.* **20**, 660-694 (2007).
8. Chan, J.F., Lau, S.K., To, K.K., Cheng, V.C., Woo, P.C. & Yuen, K.Y. Middle East respiratory syndrome coronavirus: another zoonotic betacoronavirus causing SARS-like disease. *Clin. Microbio. Rev.* **28**, 465-522 (2015).
9. World Health Organization. Weekly epidemiological update on COVID-19 - 27 April 2021. https://www.who.int/publications/m/item/weekly-epidemiological-update-on-covid-19---27-april-2021 (accessed on 1 May 2021)
10. Zumla, A., Chan, J.F., Azhar, E.I., Hui, D.S. & Yuen, K.Y. Coronaviruses - drug discovery and therapeutic options. *Nat. Rev. Drug Discovery.* **15**, 327-347 (2016).

11. Beigel, J. H. et al. Remdesivir for the Treatment of Covid-19 - Final Report. *N. Engl. J. Med.* **383**, 1813-1826 (2020).
12. Hung, I.F., et al. Triple combination of interferon beta-1b, lopinavir-ritonavir, and ribavirin in the treatment of patients admitted to hospital with COVID-19: an open-label, randomised, phase 2 trial. *Lancet*. **395**, 1695-1704 (2020).
13. Yuan, S. et al. Clofazimine broadly inhibits coronaviruses including SARS-CoV-2. *Nature*. (2021) doi: 10.1038/s41586-021-03431-4.
14. WHO Solidarity Trial Consortium et al. Repurposed Antiviral Drugs for Covid-19 - Interim WHO Solidarity Trial Results. *N. Eng. J. Med.* **384**, 497-511 (2021).
15. Liu, L. et al. Potent neutralizing antibodies against multiple epitopes on SARS-CoV-2 spike. *Nature.* **584**, 450-456 (2020).
16. Weinreich, D.M. et al. REGN-COV2, a Neutralizing Antibody Cocktail, in Outpatients with Covid-19. *N. Eng. J. Med.* **384**, 238-251 (2021).
17. Simonovich, V.A. et al. A Randomized Trial of Convalescent Plasma in Covid-19 Severe Pneumonia. *N. Eng. J. Med.* **384**, 619-629 (2021).
18. Chan, J.F. et al. Genomic characterization of the 2019 novel human-pathogenic coronavirus isolated from a patient with atypical pneumonia after visiting Wuhan. *Emerg. Microbes Infect.* **9**, 221-236 (2020).
19. Swanson, M.D., Winter, H.C., Goldstein, I.J. & Markovitz, D.M. A lectin isolated from bananas is a potent inhibitor of HIV replication. *J. Biol. Chem.* **285**, 8646-8655 (2010).
20. Coves-Datson, E.M., et al. A molecularly engineered antiviral banana lectin inhibits fusion and is efficacious against influenza virus infection in vivo. *Proc. Natl. Acad. Sci. U. S. A.* **117**, 2122-2132 (2020).
21. Coves-Datson, E.M., et al. Inhibition of Ebola Virus by a Molecularly Engineered Banana Lectin. *PLoS Negl. Trop. Dis.* **13**, e0007595 (2019).
22. Zhou, J. et al. Active replication of Middle East respiratory syndrome coronavirus and aberrant induction of inflammatory cytokines and chemokines in human macrophages: implications for pathogenesis. *J. Infect. Dis.* **209**, 1331-1342 (2014).
23. Yuan, S. et al. SREBP-dependent lipidomic reprogramming as a broad-spectrum antiviral target. *Nat. Commun.* **10**, 120 (2019).
24. Yuan, S. et al. Viruses harness YxxO motif to interact with host AP2M1 for replication: A vulnerable broad-spectrum antiviral target. *Sci. Adv.* **6**, eaba7910 (2020).
25. Chan, J.F. et al. Simulation of the Clinical and Pathological Manifestations of Coronavirus Disease 2019 (COVID-19) in a Golden Syrian Hamster Model: Implications for Disease Pathogenesis and Transmissibility. *Clin. Infect. Dis.* **71**, 2428-2446 (2020).
26. Riva, L. et al. Discovery of SARS-CoV-2 antiviral drugs through large-scale compound repurposing. *Nature.* **586**, 113-119 (2020).

27. Kodera, N., Yamamoto, D., Ishikawa, R. & Ando, T. Video imaging of walking myosin V by high-speed atomic force microscopy. *Nature.* **468**, 72-76 (2010).
28. Preiner, J. et al. IgGs are made for walking on bacterial and viral surfaces. *Nat. Commun.* **5**, 4394 (2014).
29. Hopper, J.T.S. et al. The Tetrameric Plant Lectin BanLec Neutralizes HIV through Bidentate Binding to Specific Viral Glycans. *Structure*. **25**, 773-782 e775 (2017).
30. Hinterdorfer, P., Baumgartner, W., Gruber, H.J., Schilcher, K. & Schindler, H. Detection and localization of individual antibody-antigen recognition events by atomic force microscopy. *Proc. Natl. Acad. Sci. U. S. A.* **93**,3477-3481 (1996).
31. Rankl, C. et al. Multiple receptors involved in human rhinovirus attachment to live cells. *Proc. Natl. Acad. Sci. U. S. A.* **105**, 17778-17783 (2008).
32. Bell, G.I. Models for the specific adhesion of cells to cells. *Science*. **200**, 618-627 (1978).
33. Evans, E. & Ritchie, K. Dynamic strength of molecular adhesion bonds. *Biophys. J.* **72**, 1541-1555 (1997).
34. Strnad, M., et al. Nanomechanical mechanisms of Lyme disease spirochete motility enhancement in extracellular matrix. *Commun. Biol.* **4**, 268 (2021).
35. Traxler, L., et al. Detailed Evidence for an Unparalleled Interaction Mode between Calmodulin and Orai Proteins. *Angew. Chem. Int. Ed. Engl.* **56**, 15755-15759 (2017).
36. Casalino, L. et al. Beyond Shielding: The Roles of Glycans in the SARS-CoV-2 Spike Protein. *ACS Cent. Sci.* **6**, 1722-1734 (2020).
37. Watanabe, Y., Allen, J.D., Wrapp, D., McLellan, J.S. & Crispin, M. Site-specific glycan analysis of the SARS-CoV-2 spike. *Science.* **369**, 330-333 (2020).
38. Zhao, P. et al. Virus-Receptor Interactions of Glycosylated SARS-CoV-2 Spike and Human ACE2 Receptor. *Cell Host Microbe.* **28**, 586-601 e586 (2020).
39. Hoffmann, D. et al. Identification of lectin receptors for conserved SARS-CoV-2 glycosylation sites. *bioRxiv.* 2021. doi: https://doi.org/10.1101/2021.04.01.438087.
40. O'Keefe, B.R. et al. Broad-spectrum in vitro activity and in vivo efficacy of the antiviral protein griffithsin against emerging viruses of the family Coronaviridae. *J. Virol.* **84**, 2511-2521 (2010).
41. Liu, Y.M. et al. A Carbohydrate-Binding Protein from the Edible Lablab Beans Effectively Blocks the Infections of Influenza Viruses and SARS-CoV-2. *Cell Rep.* **32**, 108016 (2020).
42. Chan, J.F. et al. Differential cell line susceptibility to the emerging novel human betacoronavirus 2c EMC/2012: implications for disease pathogenesis and clinical manifestation. *J. Infect. Dis.* **207**, 1743-1752 (2013).
43. Chu, H. et al. Comparative tropism, replication kinetics, and cell damage profiling of SARS-CoV-2 and SARS-CoV with implications for clinical manifestations, transmissibility, and laboratory studies of COVID-19: an observational study. *Lancet Microbe.* **1**, e14-e23 (2020).

44. Chan, J.F. et al. Differential cell line susceptibility to the emerging Zika virus: implications for disease pathogenesis, non-vector-borne human transmission and animal reservoirs. *Emerg. Microbes Infect.* **5**, e93 (2016).
45. Yuan, S. et al. Metallodrug ranitidine bismuth citrate suppresses SARS-CoV-2 replication and relieves virus-associated pneumonia in Syrian hamsters. *Nat. Microbiol.* **5**, 1439-1448 (2020).
46. Chan, J.F. et al. Broad-spectrum antivirals for the emerging Middle East respiratory syndrome coronavirus. *J. Infect.* **67**, 606-616 (2013).
47. Yuan, S. et al. Discovery of the FDA-approved drugs bexarotene, cetilistat, diiodohydroxyquinoline, and abiraterone as potential COVID-19 treatments with a robust two-tier screening system. *Pharmacol. Res.* **159**, 104960 (2020).
48. Zhao, H. et al. A broad-spectrum virus- and host-targeting peptide against respiratory viruses including influenza virus and SARS-CoV-2. *Nat. Commun.* **11**, 4252 (2020).
49. Chan, C.M. et al. Carcinoembryonic Antigen-Related Cell Adhesion Molecule 5 Is an Important Surface Attachment Factor That Facilitates Entry of Middle East Respiratory Syndrome Coronavirus. *J. Virol.* **90**, 9114-9127 (2016).
50. Chu, H. et al. Middle East respiratory syndrome coronavirus and bat coronavirus HKU9 both can utilize GRP78 for attachment onto host cells. *J. Biol. Chem.* **293**, 11709-11726 (2018).
51. Farkash, E.A., Wilson, A.M. & Jentzen, J.M. Ultrastructural Evidence for Direct Renal Infection with SARS-CoV-2. *J. Am. Soc. Nephrol.* **31**, 1683-1687 (2020).
52. Schindelin, J. et al. Fiji: an open-source platform for biological-image analysis. *Nat. Methods.* **9**, 676-682 (2012).
53. Lee, A.C. et al. Oral SARS-CoV-2 Inoculation Establishes Subclinical Respiratory Infection with Virus Shedding in Golden Syrian Hamsters. *Cell Rep. Med.* 1, 100121 (2020).
54. Oh, Y.J. et al. Curli mediate bacterial adhesion to fibronectin via tensile multiple bonds. *Sci. Rep.* **6**, 33909 (2016).
55. Hutter, J.L & Bechhoefer, J. Calibration of atomic-force microscope tips. *Review of Scientific Instruments.* **64**, 1868 (1993). doi.org/10.1063/1.1143970.
56. Walls, A.C., Park, Y.J., Tortorici, M.A., Wall, A., McGuire, A.T. & Veesler, D. Structure, Function, and Antigenicity of the SARS-CoV-2 Spike Glycoprotein. *Cell*. 183, 1735 (2020).
57. de Ruiter, A. & Oostenbrink, C. Protein-Ligand Binding from Distancefield Distances and Hamiltonian Replica Exchange Simulations. *J. Chem. Theory Comput.* **9**, 883-892 (2013).

Figures

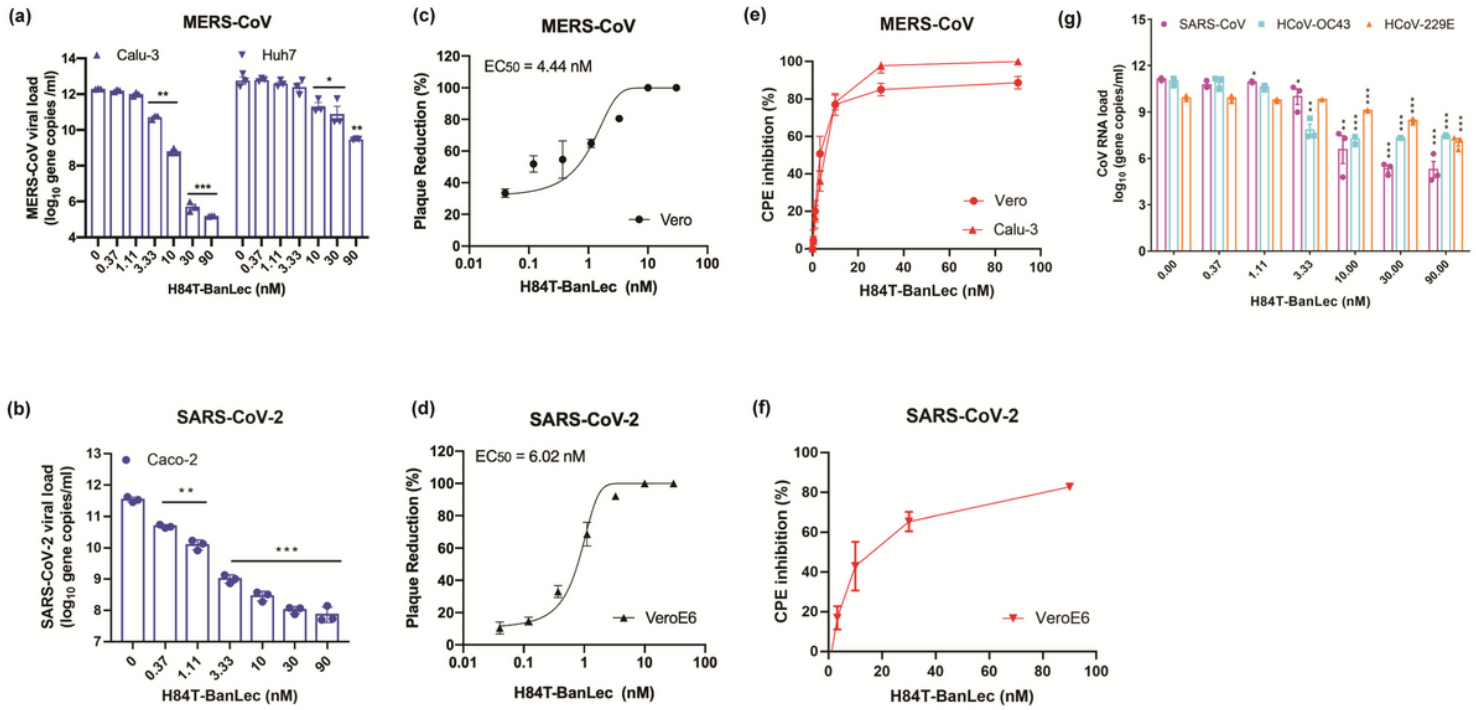

Figure 1

Broad-spectrum in vitro antiviral activity of H84T-BanLec against human-pathogenic coronaviruses. The antiviral activity of H84T-BanLec against MERS-CoV and SARS-CoV-2 (HKU-001 strain) was evaluated using (a and b) viral load reduction assay, (c and d) plaque reduction assay, and (e and f) CPE inhibition assay. g, The antiviral activity of H84T-BanLec against other human-pathogenic coronaviruses in vitro determined by viral load reduction assay for SARS-CoV (Vero cells, ATCC® CCL-81TM), HCoV-OC43 (BS-C-1 cells, ATCC® CCL-26TM), and HCoV-229E (human embryonic lung fibroblasts HFL cells, in-house development). Data are mean ± s.d., n = 3 biological replicates. One-way ANOVA. ***P<0.001, **P<0.01, *P<0.05.

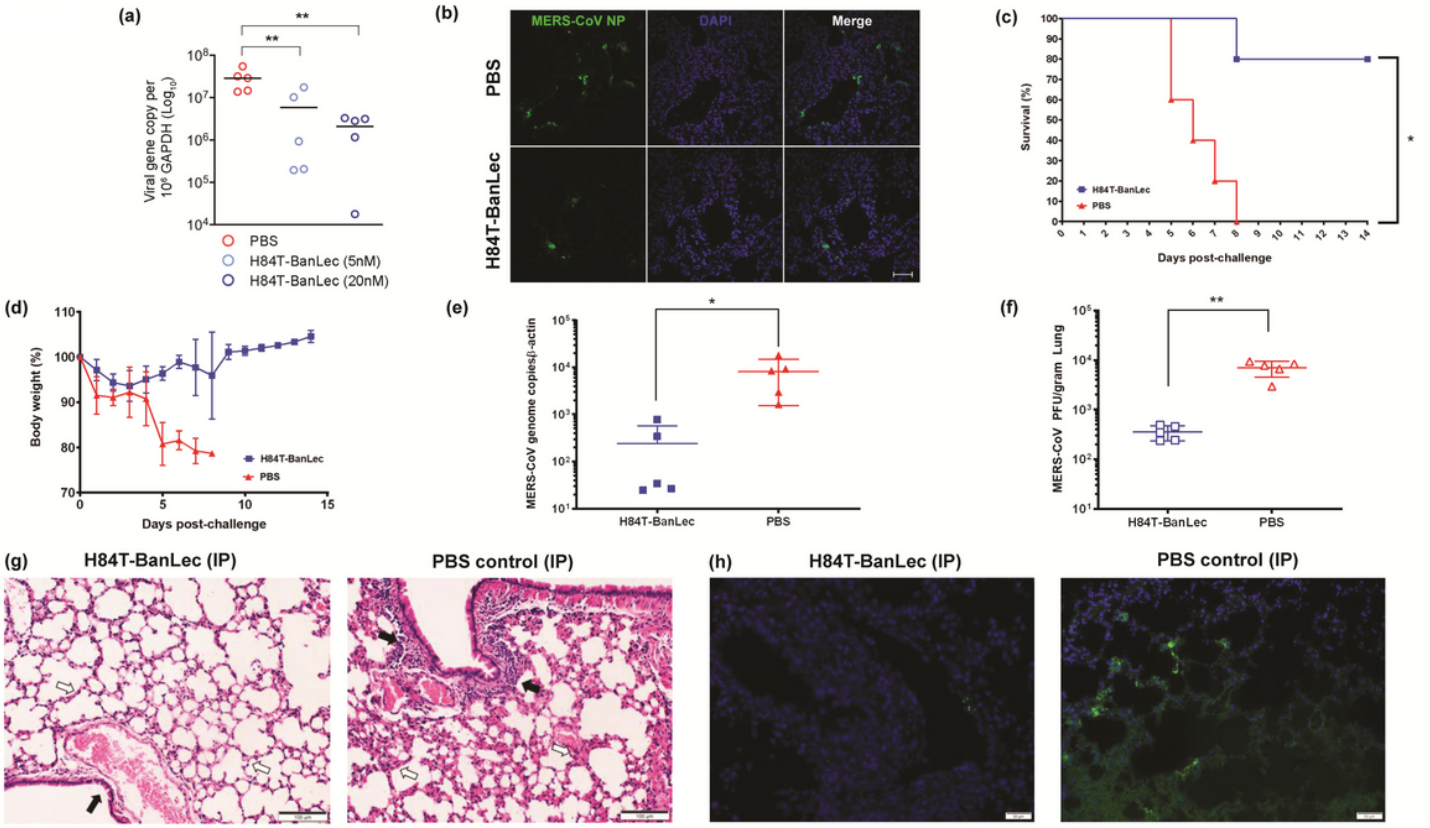

Figure 2

H84T-BanLec is highly potent against MERS-CoV in ex vivo human lung tissue organ culture and human dipeptidyl-peptidase 4 (hDPP4)-transgenic mice. a, Dose-dependent reduction of MERS-CoV viral load with increasing concentrations of H84T-BanLec treatment at 24 hpi. b, Markedly reduced MERS-CoV nucleocapsid protein (NP) expression in ex vivo human lung organ culture in H84T-BanLec-treated samples compared to PBS control-treated samples at 24 hpi. Data are mean ± s.d., n = 5 biological replicates. One-way ANOVA was used to determine significant differences in viral loads. **P<0.01. The hDPP4-transgenic mice were treated with intraperitoneal (IP 15 mg/kg/animal/day every 24h) H84T-BanLec starting at 6 hours before MERS-CoV challenge until 3 days post-infection (dpi) (n=10 per group). Five animals per group were sacrificed at 4 dpi for viral load and histopathological studies and the survival rates and body weight changes of the remaining 5 animals per group were observed until 14 dpi or death. c, Survival rates, d, body weight changes, e, viral RNA loads by qRT-PCR, and f, viral titres by plaque assay of the lungs from H84T-BanLec-treated mice versus PBS-treated mice. Data are mean ± s.d. Kaplan-Meier survival curves were analysed by the log rank test. Student's t-test was used to determine significant differences in viral loads and titers. **P<0.01, *P<0.05. Representative images of g, haematoxylin and eosin (H&E)-stained and h, immunofluorescence-stained mouse lung sections at 4 dpi with or without IP H84T-BanLec. g, The PBS-treated control mouse lung sections showed evidence of interstitial pneumonia with peribronchiolar inflammatory infiltrates (arrows) and thickened alveolar walls (open arrows). In contrast, the H84T-BanLec-treated mouse lung sections demonstrated normal bronchiolar (arrow) and alveolar (open arrows) architectures. h, Immunofluorescence staining of the PBS-

treated mouse lung sections showed abundant MERS-CoV NP expression (green) while scarce viral NP expression was observed in the lung sections of the H84T-BanLec-treated mice.

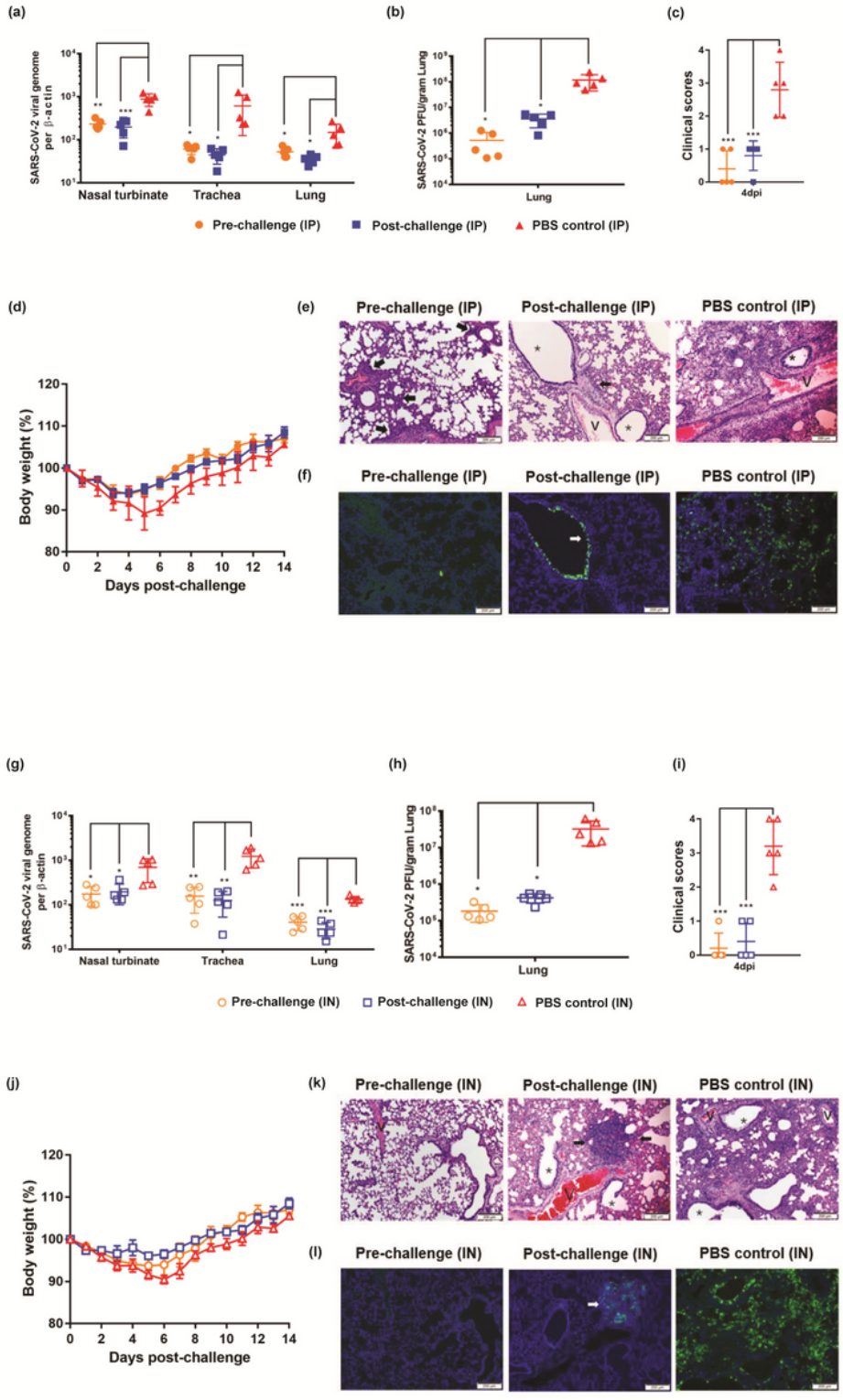

Figure 3

Intranasal or intraperitoneal H84T-BanLec reduces virus replication and alleviates histopathological changes in SARS-CoV-2-infected golden Syrian hamsters. The H84T-BanLec group hamsters were treated with (a to f) intraperitoneal (IP 15.0mg/kg/animal/day every 24h) or (g to l) intranasal (IN 1.5

mg/kg/animal/day every 24h) H84T-BanLec starting at 6h before virus challenge (pre-challenge) or 24h after virus challenge (post-challenge) until 3dpi (n=10 per group). The control hamsters were treated with (a to f) intraperitoneal or (g to l) intranasal PBS starting at 6h before virus challenge daily until 3dpi. Five animals per group were sacrificed at 4dpi for viral load and histopathological studies and the survival rates and body weight changes of the remaining 5 animals per group were observed until 14dpi or death. a, and g, SARS-CoV-2 RNA load by qRT-PCR assay in the respiratory tract tissues of the hamsters. b, and h, Quantitation of virus titre by plaque assay in the lung tissues of the hamsters. c, and i, Clinical scores and d, and j, body weight changes of the hamsters. Data are mean ± s.d. One-way ANOVA was used to determine significant differences in viral loads and titers. ***P<0.001, **P<0.01, *P<0.05. Representative images of e, H&E-stained and f, immunofluorescence-stained hamster lung sections at 4 dpi with or without IP H84T-BanLec. e, The IP PBS-treated control hamster lung sections showed prominent bronchiolar epithelial cell death (*), diffuse alveolar inflammatory infiltrates, and blood vessel (V) wall inflammatory infiltrates, with abundant SARS-CoV-2 N protein expression (green) being observed in immunofluorescence-stained lung sections. Pre-challenge IP administration of H84T-BanLec led to near-complete protection from lung damage and absence of SARS-CoV-2 NP expression except for small focal areas of mild peribronchiolar and perivascular inflammatory infiltrates (arrows). Post-challenge IP administration of H84T-BanLec also led to improved lung histopathological changes with only focal areas of bronchiolar cell death (*) with viral nucleocapsid protein expression and blood vessel inflammatory infiltrates (V). Representative images of k, haematoxylin and eosin (H&E)-stained and l, immunofluorescence-stained hamster lung sections at 4 dpi with or without IN H84T-BanLec. k, The IN PBS-treated control hamster lung sections showed bronchiolar epithelial cell death (*), diffuse lung alveolar exudation and inflammatory infiltrates, and blood vessel (V) wall inflammatory infiltrates. l, Immunofluorescence staining showed abundant and diffusely distributed SARS-CoV-2 nucleocapsid (N) protein expression (green). In stark contrast, pre-challenge IN administration of H84T-BanLec resulted in preserved lung architecture in the H&E-stained lung sections and absence of SARS-CoV-2 NP expression in immunofluorescence-stained sections. Post-challenge IN administration of H84T-BanLec similarly improved the histopathological changes in the hamster lung sections, although focal areas of mild epithelial cell death (*) and alveolar inflammatory infiltrates (arrows) that were viral NP-positive could occasionally be observed.

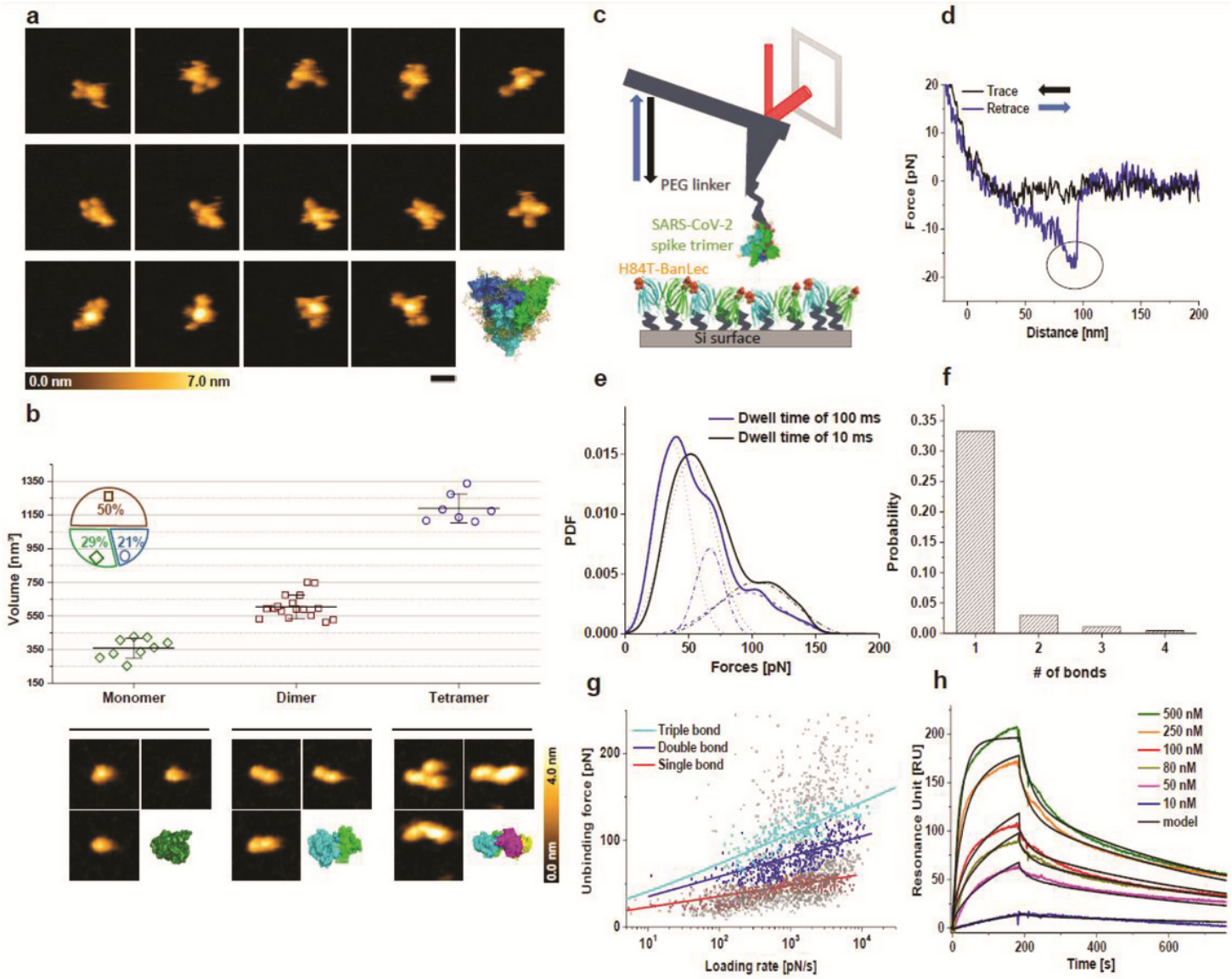

Figure 4

SARS-CoV-2 spike protein and H84T-BanLec structures and real-time observation of binding strength and affinity. a, High-speed atomic force microscopy (HS-AFM) images of single SARS-CoV-2 spike proteins. The images in the three rows were selected from movies of three independent SARS-CoV-2 spike protein molecules. The right image in the bottom row shows a fully glycosylated (yellow) 3D model of the SARS-CoV-2 trimer (green, cyan and blue). The scale bar corresponds to 25nm. b, (Top) Volume measurements of H84T-BanLec, representing a monomer, dimer and tetramer, depicted from an 886 frames movie. The inset pie chart displays the frequency distribution of oligomeric states. (Bottom) Representative HS-AFM images taken for the volume measurements and 3D surface representations of H84T-BanLec of each oligomeric state, taken from the X-ray structure (PDB: 4PIK). The scale bar corresponds to 5nm. All images were captured at a scan rate of 303ms per frame. c, Schematic design of single-molecule force spectroscopy (SMFS) experiments between full-length SARS-CoV-2 trimer coupled to an AFM cantilever tip and surface-immobilized H84T-BanLec. d, The typical force-distance curve obtained using SMFS, showing the signature of a single-bond rupture upon unbinding of the SARS-CoV-2 spike trimer from

H84T-BanLec (indicated by the circle in the retrace recording). e, Experimental probability density functions (PDFs) of unbinding forces constructed from summing up unbinding forces, each of which represented by a Gaussian of unitary area with the width of its measurement uncertainty. As such, they contain solely original data and can be viewed as the equivalent of continuous force histograms. PDFs for two different tip-surface interaction times, 100ms (blue line) and 10ms (black line), were fitted by a multi-Gaussian function. Maxima reveal rupture of a single or simultaneous rupture of 2 and 3 bonds, respectively (indicated by the numbers). f, Probability for the formation of one, two, three, or four bonds upon SARS-CoV-2 spike trimer binding to H84T-BanLec. g, Plot of unbinding force versus loading rate for SARS-CoV-2 spike trimer dissociating from H84T-BanLec. A Markov binding model computed the behavior of the double bond (blue) and triple bond (cyan) interactions, using parameters derived from the Bell and Evan's single-barrier model fit of the single bond (red). h, Surface plasmon resonance measurements. H84T-BanLec was injected (in the presence of Ca2+) at the indicated concentrations to surfaces containing immobilized full-length trimeric spike to allow for binding (ascending parts), followed by wash out using buffer (descending parts). Data were fitted using the bivalent binding model, consistent with H84T-BanLec being predominantly a dimer.

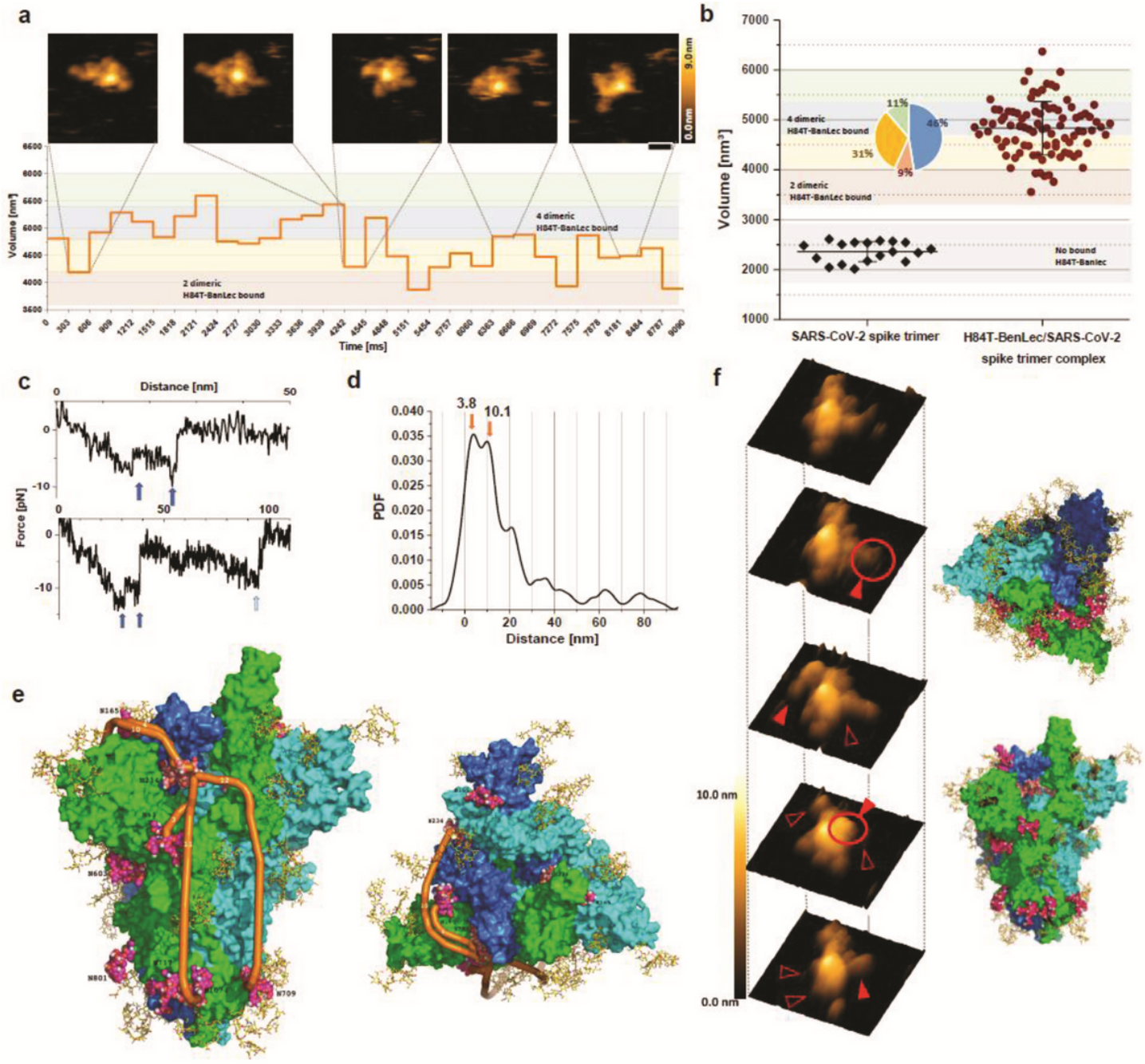

Figure 5

Structure and dynamics of multiple bonds formed between SARS-CoV-2 spike protein and H84T-BanLec. a, High-speed atomic force microscopy (HS-AFM) frames of a single SARS-CoV-2 spike trimer complexed with H84T-BanLec. The scale bar corresponds to 25nm. All images were captured at a scan rate of 303ms per frame. The graph in the lower part displays the variation of the volume over time. Volume ranges indicative of the number of dimeric H84T-BanLec molecules bound to the SARS-CoV-2 spike protein are marked by colours in the background. b, Volume measurements of isolated SARS-CoV-2 spike protein and SARS-CoV-2 spike protein complexed with H84T-BanLec. The volumes of isolated SARS-CoV-2 spike protein were determined from 18 frames taken from three different movies. Volumes of SARS-CoV-2 spike protein associated with H84T-BanLec were taken from 3 different individual H84T-BanLec/SARS-CoV-2

spike complexes of 30 frames each. The colours in the background of the graph indicate the number of dimeric H84T-BanLec molecules bound and the inset pie chart displays their frequency distribution (same colour code as background). c, Examples of SMFS force-distance curves containing two or three sequential bond ruptures, respectively, upon unbinding of SARS-CoV-2 spike protein from H84T-BanLec (indicated with blue arrows). d, Distribution of distances of sequential bond ruptures (as exemplified in c), represented by an experimental probability density function of distances constructed from distance values measured by SMFS (main maxima at 3.8+0.5nm and 10.1+0.8nm). e, Left: 3D structural model of SARS-CoV-2 spike trimer with monomers in green, cyan and blue. Complex-type glycans in yellow; high-mannose glycan (Man9) on N234 space filling with salmon carbons, oligo-mannose glycans (Man5) space filling with carbons in magenta. The shortest curved paths are indicated in orange [Man9 on N234 to Man9 on N234 (second monomer), Man5 on N61, Man5 on N709, and Man5 on N1074]. Right: 3D structural model of SARS-CoV-2 spike trimer interacting with H84T-BanLec dimer in orange. f, Structures of the H84T-BanLec/SARS-CoV-2 spike complex shown with 3D representations of HS-AFM topographical images. The filled red arrows and empty arrows indicate association and dissociation of H84T-BanLec with the SARS-CoV-2 spike protein, respectively. 3D structural models of the SARS-CoV-2 spike trimer from side view (bottom) and with the RBD pointing down (top) with Man5/Man9 glycans on one monomer highlighted are shown to the right. The dynamics of H84T-BanLec association and dissociation are displayed in Supplementary Video S1.

Supplementary Files

This is a list of supplementary files associated with this preprint. Click to download.

- SupplementaryVideoS120210508.avi
- ExtendedDataFiguresandLegends20210508.pdf